The Astronomical Journal, 171:20 (15pp), 2026 January https://doi.org/10.3847/1538-3881/ae1b91

TESS Investigation—Demographics of Young Exoplanets (TI-DYE). IV. A Jovian-radius Planet Orbiting a 34 Myr Sun-like Star in the Vela Association

Madyson G. Barber[1,14], Andrew W. Mann[1], Andrew Vanderburg[2,3], Khalid Barkaoui[4,5,6], Karen A. Collins[2], Sebastian Carrazco-Gaxiola[7,8], Phil Evans[9], Matthew J. Fields[1], Michaël Gillon[5], Todd J. Henry[8], Katharine M. Hesse[3], Wei-Chun Jao[7], Emmanuel Jehin[10], Sydney Jenkins[3], Tim Johns[7,8], David R. Rodriguez[11], Richard P. Schwarz[2], William C. Storch[1], Cristilyn N. Watkins[12], and Francis P. Wilkin[13]

[1] Department of Physics and Astronomy, The University of North Carolina at Chapel Hill, Chapel Hill, NC 27599, USA; madysonb@live.unc.edu
[2] Center for Astrophysics | Harvard & Smithsonian, 60 Garden Street, Cambridge, MA 02138, USA
[3] Department of Physics and Kavli Institute for Astrophysics and Space Research, Massachusetts Institute of Technology, Cambridge, MA 02139, USA
[4] Instituto de Astrofísica de Canarias (IAC), E-38200, La Laguna, Tenerife, Spain
[5] Astrobiology Research Unit, Université de Liège, B-4000 Liège, Belgium
[6] Department of Earth, Atmospheric and Planetary Science, Massachusetts Institute of Technology, Cambridge, MA 02139, USA
[7] Department of Physics and Astronomy, Georgia State University, Atlanta, GA 30302, USA
[8] RECONS Institute, Chambersburg, PA 17201, USA
[9] Phil Evans, El Sauce Observatory, Coquimbo Province, Chile
[10] Space Sciences, Technologies and Astrophysics Research (STAR) Institute, Université de Liège, B-4000 Liège, Belgium
[11] Space Telescope Science Institute, 3700 San Martin Drive, Baltimore, MD 21218, USA
[12] Bozeman, MT 59718, USA
[13] Department of Physics and Astronomy, Union College, 807 Union Street, Schenectady, NY 12308, USA

Received 2025 September 2; revised 2025 October 17; accepted 2025 October 31; published 2025 December 9

Abstract

The discovery of infant (<50 Myr), close-in (<30-day-period) planets is vital in understanding the formation mechanisms that lead to the distribution of mature transiting planets as discovered by Kepler. Despite several discoveries in this age bin, the sample is still too small for a robust statistical comparison to older planets. Here we report the validation of TOI-6448b, an $8.8 \pm 0.8\,R_\oplus$ planet on a 14.8-day orbit. TOI-6448 was previously identified to be a likely member of Vela Population IV. We confirm the star's membership and rederive the age of the cluster using isochrones, variability, and gyrochronology. We find the star, and thus planet, to be 34 ± 3 Myr. Like other young planets, TOI-6448 b lands in a region of parameter space with few older planets. While just one data point, this fits with prior findings of an excess of 5–11 $R_\oplus$ planets around young stars far beyond what can be explained by reduced sensitivity at young ages. Our ongoing searches of Vela, Taurus-Auriga, Sco-Cen, and Orion are expected to reveal dozens more <50 Myr transiting planets.

Unified Astronomy Thesaurus concepts: Exoplanets (498); Young star clusters (1833); Transit photometry (1709); Transits (1711); Young stellar objects (1834)

Materials only available in the online version of record: machine-readable table

1. Introduction

Despite dozens of discoveries of planets <500 Myr, theories surrounding which formation mechanisms are dominant in reproducing the Kepler distribution are largely not understood. Two such pathways, the gas dwarfs versus water world formation, model sub-Neptunes and super-Earths as forming from the cores of young planets with once large, extended atmospheres (e.g., E. J. Lee et al. 2014; S. Ginzburg et al. 2016) or maintaining consistent radii through time owing to thinner, higher mean molecular weight atmospheres (e.g., C. Mordasini et al. 2009; J. Venturini et al. 2016; L. Zeng et al. 2019; R. Burn et al. 2024).

Testing these theories requires an understanding of the young planet population, as planets begin to lose markers of their formation quickly after the protoplanetary disk gas dissipates (∼3–10 Myr; e.g., S. J. Kenyon & L. Hartmann 1995; C. M. Koepferl et al. 2013; J. G. Rogers et al. 2024). Mass measurements, while able to distinguish between a true sub-Neptune and a super-Earth (e.g., Y. Wu & Y. Lithwick 2013; A. Wolfgang et al. 2016; R. Luque & E. Pallé 2022), are difficult for young planets. Masses via radial velocities (RVs) are complicated by stellar jitter (e.g., S. Blunt et al. 2023), and masses through transit timing variations (TTVs) require detecting all major perturbing bodies (small planets may elude detection owing to young stellar noise or poor photometric precision, affecting the TTV analysis; e.g., D. Weisserman et al. 2023) and rely on the system having multiple coplanar orbiting objects. Although transmission spectroscopy with JWST has been successful in obtaining mass measurements of young planets (J. de Wit & S. Seager 2013; S. Barat et al. 2024; P. C. Thao et al. 2024), obtaining enough mass measurements to test formation theories would require an intense observational campaign. These measurements can also be challenging for young sub-Neptunes, whose higher masses can mute spectral features.

Instead, we can look at planet radii over time to approximate a typical evolution trajectory. For planet radii to be successful in differentiating the gas dwarf and water world scenarios, we rely heavily on understanding the youngest population

---

[14] NSF Graduate Research Fellow.

($<$50 Myr), where these formation pathways are most divergent (e.g., J. G. Rogers 2025). Even with multiple discovered systems in this age bin (e.g., V1298 τ, HIP 67522, NGST 33, TIC 88785435; T. J. David et al. 2019a, 2019b; A. C. Rizzuto et al. 2020; M. G. Barber et al. 2024b; D. R. Alves et al. 2025; S. Vach et al. 2025) and a distribution suggestive of a gas-dwarf-dominated formation scenario (S. Vach et al. 2024), we do not have *enough* planets for a statistically significant differentiation between the two proposed pathways. This is further challenged by a number of these youngest planets orbiting fainter or more distant stars (e.g., K2-33, TOI-1227, Kepler-1975, IRAS 04125+2902; A. W. Mann et al. 2016b, 2022; L. G. Bouma et al. 2022; M. G. Barber et al. 2024a), which can complicate follow-up efforts.

A major goal of the TESS Investigation—Demographics of Young Exoplanets (TI-DYE) survey (see M. G. Barber et al. 2024a, 2024b) is discovering and characterizing the youngest transiting systems in order to test these formation pathways. The focus is on systems younger than 50 Myr, where planet models make divergent predictions (e.g., A. Karalis et al. 2025; J. G. Rogers 2025), and before post-formation evolution erases information about a planet's initial conditions (K. Marimbu & E. J. Lee 2024). A connected part of the survey is to find additional planets in known, young, transiting systems (e.g., M. G. Barber et al. 2025), as multitransiting systems are similarly powerful for testing models of planetary evolution (e.g., F. Dai et al. 2024).

In this paper, we validate the detection of TOI-6448 b. We describe the observations of the system in Section 2 and the planet detection in Section 2.1.1. In Sections 3 and 4, we derive the star and planet properties, respectively, and we perform an injection–recovery analysis in Section 5. We discuss false-positive scenarios in Section 6. We use the list of comoving stars identified in Section 7.1 to derive a precise age for the system in Section 7.3. Finally, we discuss the importance of this system and continued work in Section 8.

2. Observations

2.1. TESS Light Curve

TOI-6448 (TIC 320411045) was first observed by TESS in Sector 33 from 2020 December 18 to 2021 January 13 and reobserved in sectors 34 (2021 January 14–2021 February 8), 61 (2023 January 18–2023 February 12), and 87 (2024 December 18–2025 January 14). For Sector 87, the target was observed in short-cadence (20-s and 2 minute light curves), and in the remaining sectors, the target was only observed in TESS full frame images. The TESS data used in this analysis can be found in MAST (TESS Team 2021, 2022).

We built our TESS light curve following M. G. Barber et al. (2024a), which was an update of the extraction and systematic corrections of A. Vanderburg et al. (2019).[15] This method has been used effectively on young variable stars with transiting planets (e.g., M. G. Barber et al. 2024a; B. K. Capistrant et al. 2024; P. C. Thao et al. 2024). We always use the light curve with the fastest cadence available for each sector.

2.1.1. Planet Detection

The Quick-Look Pipeline (QLP) faint-stars search (M. Kunimoto et al. 2022) of sectors 33, 34, and 61 identified a 14.8-day signal, which was released as TOI-6448.01 on 2023 May 3.

We ran the updated `Notch & LOCoR` (`N&L`; A. C. Rizzuto et al. 2017) as described in M. G. Barber et al. (2024a). Using a 0.5-day filtering window, we used `Notch` to detrend the light curve with a second-order polynomial while preserving trapezoidal, transit-like shapes. As it detrends the light curve, for every point, `Notch` calculates the change in the Bayesian information criterion (BIC) based on how well adding the trapezoid to the polynomial improved the model. We then implemented a box least-squares (BLS) search on the BIC time series to search for periodic signals between 0.5 and 30 days with a signal-to-noise ratio (SNR) $>$ 8. We recovered the 14.8-day signal with a BLS SNR of 33. The detected period, initial transit time, and depth matched that of the TESS QLP detection. No other planet-like signals were detected with periods of 0.5–30 days.

2.2. Ground-based Photometry

The TESS pixel scale is $\sim$21$''$ pixel^{-1}, and photometric apertures typically extend out to roughly 1$'$, generally causing multiple stars to blend in the TESS photometric aperture. Multiwavelength observations of the transit are also useful for false-positive vetting. To these ends, we acquired ground-based time-series follow-up photometry of the field around TOI-6448 as part of the TESS Follow-up Observing Program (TFOP; K. Collins 2019).[16]

2.2.1. LCOGT

We observed an ingress window and a full transit window of TOI-6448.01 on UTC 2024 November 25 and UTC 2024 December 9, respectively, in Sloan g' band from Las Cumbres Observatory Global Telescope (LCOGT; T. M. Brown et al. 2013) 0.35ṁ network nodes. The November light curve was observed from Teide Observatory on the island of Tenerife (TEID), and the December light curve was observed from South Africa Astronomical Observatory (SAAO) near Sutherland, South Africa. The 0.35 m Planewave Delta Rho 350 telescopes are equipped with a 9576 × 6388 QHY600 CMOS camera that has an image scale of $0\overset{''}{.}73$ pixel^{-1}, resulting in a 114$'$ × 72$'$ full field of view. We used the optional 30$'$ × 30$'$ subfield of view for a faster detector readout.

The images were calibrated by the standard LCOGT `BANZAI` pipeline (C. McCully et al. 2018), and differential photometric data were extracted using `AstroImageJ` (K. A. Collins et al. 2017). We used circular $8\overset{''}{.}7$ and $3\overset{''}{.}7$ photometric apertures for the November and December observations, respectively. We detected the transit in the target star photometric aperture in both light curves, which confirms that the TESS-detected event is indeed occurring in TOI-6448. Furthermore, the Sloan g'-band transit depth is consistent with the transit depths in the redder TESS band and other follow-up bands (see Section 4).

---

[15] We call these VanderCurves.

[16] https://tess.mit.edu/followup

Table 1
Radial Velocity Measurements of TOI-6448 Taken in This Work

Epoch (BJD)	RV (km s^{-1})	$\sigma_{\rm RV}$ (km s^{-1})	Instrument
2,460,819.467	21.40	1.05	CHIRON
2,460,822.459	21.34	2.03	MIKE
⋯	19.10	2.06	Gaia DR3

Note. The Gaia RV is listed for reference.

2.2.2. *TRAPPIST-South*

We used the TRAPPIST-South (TRAnsiting Planets and PlanetesImals Small Telescope; M. Gillon et al. 2011; E. Jehin et al. 2011) telescope to observe a full transit of TOI-6448.01 on UT 2024 February 17. TRAPPIST-South is a 0.6 m Ritchey–Chrétien telescope located at La Silla Observatory in Chile, and it is equipped with a 2K × 2K FLI Proline CCD camera with a pixel scale of $0''.65$ and a $22' \times 22'$ field of view. The observations were conducted in the $I + z$ filter with an exposure time of 50 s. During the observations of the target, the telescope underwent a meridian flip at BJD 2,460,357.601.

Data reduction and photometric extraction were performed using the `AstroImageJ` (K. A. Collins et al. 2017) software using a 9-pixel ($6''.6$) aperture radius. As with LCO, the transit was clearly visible and exhibited a depth consistent with the TESS transits.

2.2.3. *El Sauce*

We observed a full transit in Johnson–Cousins R_c band on UT 2024 February 17 using the Evans 0.51 m telescope at El Sauce Observatory in Coquimbo Province, Chile. The telescope was equipped with a Moravian C3-26000 camera with resolution 6252 × 4176 pixels. After binning 2 × 2 in camera, the resulting image scale was $0''.449$ pixel^{-1}. The photometric data were obtained from 150 × 120 s exposures, after standard calibration, using a circular $5''.4$ aperture in `AstroImageJ` (K. A. Collins et al. 2017). The transit depth was consistent with the TESS transits.

2.3. *Ground-based Spectroscopy*

2.3.1. *CHIRON*

We observed TOI-6448 on UT 2025 May 23 using the CHIRON echelle spectrometer on the SMARTS 1.5 m telescope at the Cerro Tololo Inter-American Observatory in Chile. The exposure was 20 minutes and utilized the fiber mode. CHIRON fiber mode covers 4100–8700 Å with a resolution $R \sim 25{,}000$. We reduced the data using the CHIRON data reduction pipeline (A. Tokovinin et al. 2013; L. A. Paredes et al. 2021).

We extract the RV by cross-correlating the continuum-normalized spectra to PHOENIX model spectra (5900 K, $\log g = 4.5$; T.-O. Husser et al. 2013) and correcting for barycentric motion using `barycorrpy` (J. T. Wright & J. D. Eastman 2014). For RVs, we used orders with strong absorption features (e.g., Ca II, Li, H, He, and K) and adopted the median value and standard deviation as the RV for this epoch (Table 1).

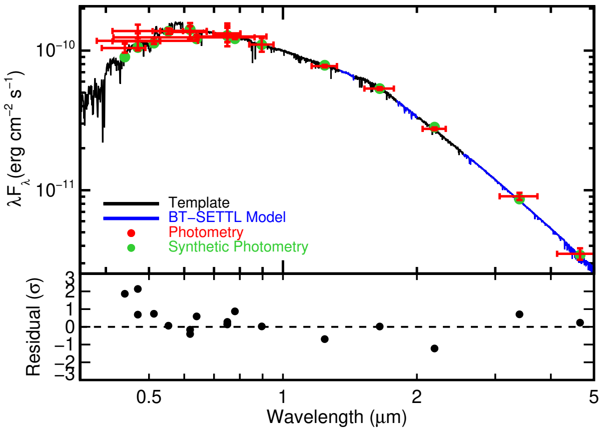

Figure 1. Fit to the SED of TOI-6448, showing the best-fit template (black) filler model (blue), observed photometry (red), and synthetic photometry (green). For the photometry, the vertical error bars are the photometric uncertainties, while the horizontal error bars represent the filter width. The bottom panel shows the residuals in units of standard deviations. The fit is marginalized over a range of templates and extinctions; this one is a G1.5V with low extinction ($A_V = 0.05$).

2.3.2. *MIKE*

We observed TOI-6448 on UT 2025 May 26 using the Magellan Inamori Kyocera Echelle (MIKE; R. Bernstein et al. 2003) instrument on the Magellan Clay telescope at the Las Campanas Observatory in Chile using the $1''.0$ slit and both arms (red ($R \sim 22{,}000$) and blue ($R \sim 28{,}000$)) simultaneously, covering 3350–9500 Å. We reduced the 15-minute exposure using the CarPy MIKE pipeline (D. D. Kelson et al. 2000; D. D. Kelson 2003).

Repeating the same processes as for the CHIRON spectra, we cross-correlate the continuum-normalized spectra to PHOENIX model spectra, using only orders with strong stellar absorption features and correcting for barycentric motion. We again adopt the median value and standard deviation (across both arms) as the reported value for this epoch.

3. Stellar Properties

3.1. $T_{\rm eff}$, L_*, *and* R_* *from the SED*

We fit the spectral energy distribution (SED) of TOI-6448 following A. W. Mann et al. (2016b). Specifically, we gathered photometry from M. F. Skrutskie et al. (2006), A. A. Henden et al. (2012), R. M. Cutri et al. (2014), C. Wolf et al. (2018), or D. W. Evans et al. (2018). We compared the photometry to a grid of flux-calibrated templates from S. R. Heap & D. J. Lindler (2007), J. T. Rayner et al. (2009), and A. Villaume et al. (2017), which have been supplemented with optical or near-IR flux-calibrated spectra where available (A. W. Mann et al. 2013; E. Gaidos et al. 2014). The templates generally span 0.36–2.4 μm, but we used PHOENIX BT-SETTL atmosphere models (F. Allard et al. 2013) to fill from 2.4 to 20 μm and a few regions of high telluric contamination.

To compute $F_{\rm bol}$, we integrated the resulting absolutely calibrated spectrum and turned this into L_* using the Gaia DR3 parallax. We estimated $T_{\rm eff}$ from the BT-SETTL model fit and R_* from the Stefan–Boltzmann relation, as well as the scaling of the model to the data (Infrared Flux Method; D. E. Blackwell & M. J. Shallis 1977).

Table 2
Stellar Parameters of TOI-6448

Parameter	Value	Source
Identifiers		
TOI	6448	TESS
TIC	320411045	TESS
Gaia	5590921485126584832	Gaia DR3
	Astrometry	
α	110.170410	Gaia DR3
δ	−33.922328	Gaia DR3
μ_α (mas yr^{-1})	−8.021 ± 0.010	Gaia DR3
μ_δ (mas yr^{-1})	5.0780 ± 0.0128	Gaia DR3
π (mas)	2.637 ± 0.011	Gaia DR3
	Photometry	
TESS (mag)	12.3239 ± 0.0061	TESS
G (mag)	12.7708 ± 0.0029	Gaia DR3
B_P (mag)	13.1151 ± 0.0040	Gaia DR3
R_P (mag)	12.2579 ± 0.0043	Gaia DR3
	Physical Properties	
$v \sin i_*$ (km s^{-1})	20.5 ± 1.7	This work
i_* (deg)	>70	This work
$P_{\rm rot}$ (days)	2.412 ± 0.037	This work
$F_{\rm bol}$ (erg cm^{-2} s^{-1})	(2.00 ± 0.12) × 10^{-10}	This work
$T_{\rm eff}$ (K)	5910 ± 90	This work
A_V (mag)	$0.06^{+0.06}_{-0.04}$	This work
R_* ($R_\odot$)	0.897 ± 0.07	This work
M_* ($M_\odot$)	1.03 ± 0.05	This work
ρ_* ($\rho_\odot$)	1.43 ± 0.37	This work
L_* ($L_\odot$)	0.908 ± 0.068	This work
Age (Myr)	34 ± 3	This work

As we show in Figure 1, the overall fit to the photometry was excellent; the best fit had a $\chi^2_\nu \lesssim 1$ with no sign of systematics with wavelength. The resulting parameters were $F_{\rm bol} = (2.00 \pm 0.12) \times 10^{-10}\,{\rm erg\,cm^{-2}\,s^{-1}}$, $L_* = 0.908 \pm 0.068\ L_\odot$, $T_{\rm eff} = 5910 \pm 90\,{\rm K}$, and $R_* = 0.897 \pm 0.070\ R_\odot$. We found extinction to be low ($A_V < 0.15$), with some templates reproducing the photometry without any extinction corrections. Final parameters are reported in Table 2.

3.2. M$_*$ from T$_{eff}$ and Age

We estimate the stellar mass following the procedure in M. J. Fields et al. (2025). To summarize, `stelpar`[17] simultaneously fits for stellar mass (M_*), age, extinction (A_V), and underestimated uncertainties (f) by comparing observed photometry to evolutionary model grids in a Markov Chain Monte Carlo (MCMC) framework. We ran `stelpar` against the DSEP-magnetic (G. A. Feiden 2016) and PARSEC (A. Bressan et al. 2012) models, placing a prior on $T_{\rm eff}$ ($T_{\rm eff} = 5910 \pm 90$ K) and a loose prior on age (30 ± 10 Myr; see Section 7.3). The model also produces a stellar radius, which we can compare to our SED fit as a check. The DSEP-magnetic model produced $M_* = 1.12 \pm 0.03\ M_\odot$, $A_V = 0.46 \pm 0.2$, and $R_* = 1.09 \pm 0.03\ R_\odot$, while the PARSEC model produced $M_* = 1.03 \pm 0.01\ M_\odot$, $A_V = 0.06^{+0.06}_{-0.04}$, and $R_* = 0.92 \pm 0.01\ R_\odot$. Due to the stellar radius and extinction agreeing with the SED fit, we choose to adopt the PARSEC model for our stellar mass.

Based on a comparison to young stars with transit-based densities, M. J. Fields et al. (2025) recommend maintaining a minimum uncertainty of 5% on the produced values (see also J. Tayar et al. 2022), so we report a final stellar mass of $M_* = 1.03 \pm 0.05\ M_\odot$. For R_*, we use the value from the SED fit (Section 3.1), which we note agrees well with the PARSEC radius ($<1\sigma$) and marginally with the DESP-mag radius (2.5σ).

3.3. Rotational Broadening and Stellar Inclination

We estimate the rotational broadening ($v \sin i_*$) of TOI-6448 by cross-correlating the observed MIKE and CHIRON spectra with the PHOENIX model spectra. We adapted the procedure (and associated code[18]) from A. Y. Kesseli et al. (2018), with minor updates described in M. J. Fields et al. (2025). To summarize, we artificially broadened the slow-rotating PHOENIX model spectra using a grid of $v \sin i_*$ values linearly spaced from 2 to 50 km s^{-1} and cross-correlated each with the observed spectra. We then measure the full width at half-maximum of the cross-correlation function to determine the $v \sin i_*$. We repeat this process for each instrument, using the same orders used to find the RVs in Sections 2.3.1 and 2.3.2. We drop three values that disagreed with the remaining 12 orders (likely due to stronger tellurics and weaker stellar lines).

Taking the median and standard deviation of the 12 $v \sin i_*$ measurements, we determine $v \sin i_* = 20.5 \pm 1.7\ {\rm km\,s^{-1}}$. We find that perturbing the model metallicity (−0.5, 0.5), log g (4.0, 5.0), and temperature (5800, 6000 K) did not significantly alter the $v \sin i_*$ measurement outside of uncertainties.

Following K. Masuda & J. N. Winn (2020) and using the associated code from M. J. Fields et al. (2025),[19] we estimate the stellar inclination (i_*) from $v \sin i_*$. Taking into account the uncertainties in the rotation period (calculated with the rest of the identified comoving stars in Section 7.3.3), stellar radius, and $v \sin i_*$, we find $i_* > 70°$ at 1σ ($i_* > 62°$ at 2σ). This is consistent with edge-on stellar rotation, as we expect if the planet is aligned with the host.

4. Planet Properties

4.1. TESS Transit Fit

We fit the systematic-corrected TESS light curves using MCMC Interface for Synthesis of Transits, Tomography, Binaries, and Others of Relevant Nature (MISTTBORN; A. W. Mann et al. 2016a; M. C. Johnson et al. 2018).[20] `MISTTBORN` simultaneously fits for the planet and stellar variability using `BATMAN` transit models (L. Kreidberg 2015) and a `celerite2` Gaussian process (GP; D. Foreman-Mackey 2018) in an MCMC framework using `emcee` (D. Foreman-Mackey et al. 2013).

We opted to use stochastically driven damped simple harmonic oscillators (SHOs) for modeling stellar variability, as suggested by D. Foreman-Mackey et al. (2017). This has also been used widely on prior analyses of young transiting planets with TESS (e.g., E. A. Gilbert et al. 2022; M. L. Wood et al. 2023; P. C. Thao et al. 2024). It is common to use a mixture of

---

[17] https://github.com/mjfields/stelpar

[18] https://github.com/aurorayk/Vsini

[19] https://github.com/mjfields/cosi

[20] https://github.com/captain-exoplanet/misttborn

Table 3
Priors Used in the `MISTTBORN` TESS Transit Fit

Description	Parameter	Prior[a]
	Planet Parameters	
Impact parameter	b	U (0.0, 1.0)
Planet-to-star radius ratio	R_P/R_*	U (0.0, 1.0)
	Stellar Parameters	
Limb-darkening coefficient	$q1$	U (0.0, 1.0)
Limb-darkening coefficient	$q2$	U (0.0, 1.0)
Stellar density	ρ_* ($\rho_\odot$)	N (1.42, 0.37)
	GP Parameters	
Period	P (days)	$P > 0$
Damping timescale	τ (days)	$\tau > P$
Standard deviation	σ	$\sigma > 0$

Note.
[a] $U(a, b)$ indicates a uniform distribution from a to b. $N(a, b)$ indicates a normal distribution centered at a with a standard deviation of b.

two SHOs (SHOM or SHOMixture), one at the characteristic period and one at half or double that period. However, we found that the second SHO was unconstrained, while a single SHO was sufficient to model the stellar variability over the whole light curve.

We fit for 12 parameters in total. For the planet, we fit for the time of inferior conjunction (T_0), orbital period (P), planet-to-star radius ratio (R_P/R_*), and impact parameter (b). We additionally fit for $\sqrt{e}\cos\omega$ and $\sqrt{e}\sin\omega$ to determine orbital eccentricity (e) and the argument of periastron (ω). For the star, we fit for stellar density (ρ_*) and two quadratic limb-darkening coefficients (q_1 and q_2) following the triangular sampling prescription (D. M. Kipping 2013). The remaining parameters were used in the GP model: the undamped period of the oscillator (P), the damping timescale (τ), and the standard deviation of the process (σ).

Most parameters evolved under uniform priors with only physical limitations, with the exception of ρ_*, which evolved under a Gaussian prior for one of the two fits (see Table 3). Transit duration is affected by both the stellar density and orbital eccentricity (V. Van Eylen & S. Albrecht 2015). We initially ran the fit assuming a circular orbit (locking $e = 0$) and allowing ρ_* to float (with a lower limit of 0). We found that the stellar density disagreed with the expected value from the stellar mass and radius (1.43 ± 0.37 $\rho_\odot$), suggesting that the orbit is eccentric. We opted to rerun the fit letting eccentricity float and placing the Gaussian prior on ρ_*.

We ran the MCMC for both fits ($e = 0$ and e-float) with 50 walkers for 100,000 steps and a 20% burn-in. The total run time was more than 50 times the autocorrelation time, indicating that the number of steps was sufficient for convergence (J. Goodman & J. Weare 2010).

We show the phase-folded light curve and representative section of the light curve and model in Figure 2 and list the best-fit parameters in Table 4. For both fits, all parameters agreed with one another, with the exception of the stellar density. Due to the high disagreement between the stellar density from the transit fit and the stellar density from the mass and radius, we prefer the eccentric transit fit (see Figure 3).

4.2. Ground-based Transit Fit

We fit the ground-based photometry separate from the TESS data. Our main goal with the ground-based data is to confirm that the transit timing and depth are consistent and that the transit is occurring on-source (i.e., for false-positive assessment).

Two of the ground-based transits (R_C and $I + z$ filters) were taken simultaneously. This is ideal for checking the transit depth, as we do not have to worry about changing spot properties or other effects that vary on week-to-month timescales, and lets us lock to a common T_0.

We fit the photometry using a `BATMAN` transit model and a second-order polynomial to handle stellar variability. The baseline for the photometry was too narrow to train a periodic GP, and the photometry (including the TESS photometry) is well described by a simple polynomial over windows of <0.5 days (Figure 2). The second-order polynomial had the form

$$f_{\text{corrected}} = f_{\text{raw}} - (a + b \times t + c \times t^2), \tag{1}$$

where t is the number of days since the first data point (to keep all values positive).

Since we are only interested in constraining the transit depth and timing, we lock all planet parameters to the TESS fit with the exception of R_P/R_* and T_0. We locked limb-darkening coefficients for each filter using values determined with `LDTK` (H. Parviainen & S. Aigrain 2015). For the simultaneous transits, we fit the transits with the same T_0 but independent R_P/R_* and variability models (to account for differences in telescope systematics and data reduction). The two g' transits were fit independently of the two simultaneous transits and fit using a common R_P/R_* but separate T_0 and variability parameters.

As above, we ran the MCMC using 50 walkers with 50,000 steps and a 20% burn-in. We show the resulting fit in Figure 4 and present the best-fit parameters in Table 5. As can be seen in Figure 4(e), all transit depths are consistent with each other at 1σ.

4.3. Global Analysis

To achieve the most precise transit parameters, we reran our `MISTTBORN` transit fit using the TESS and ground-based photometry. We opted to use the same priors and GP kernel as the TESS-only fit (Section 4.1), with the exception of an additional Gaussian prior to all limb-darkening coefficients (±0.1).

We model variability in both TESS and ground-based data with the same SHO kernel. This works if the dominant source of variability in each dataset is the rotation signal. While the ground-based data also contain instrumental and atmospheric effects, in practice these are small compared to the variability signal (Figure 2), and the data gaps allow the GP to adjust to the newer dataset. One GP does, however, prevent us from using simultaneous datasets, so we removed the R_c data in favor of the more precise $I + z$ data.

We fit for 16 parameters in total. For the four datasets (TESS, $I + z$, and two g'), we use six common parameters to describe the transit (T_0, period, R_P/R_*, b, $\sqrt{e}\sin\omega$, and $\sqrt{e}\cos\omega$), three common parameters to describe the SHO GP kernel (period, τ, and σ), and a common stellar density (ρ_*). For each filter, we fit for two limb-darkening coefficients.

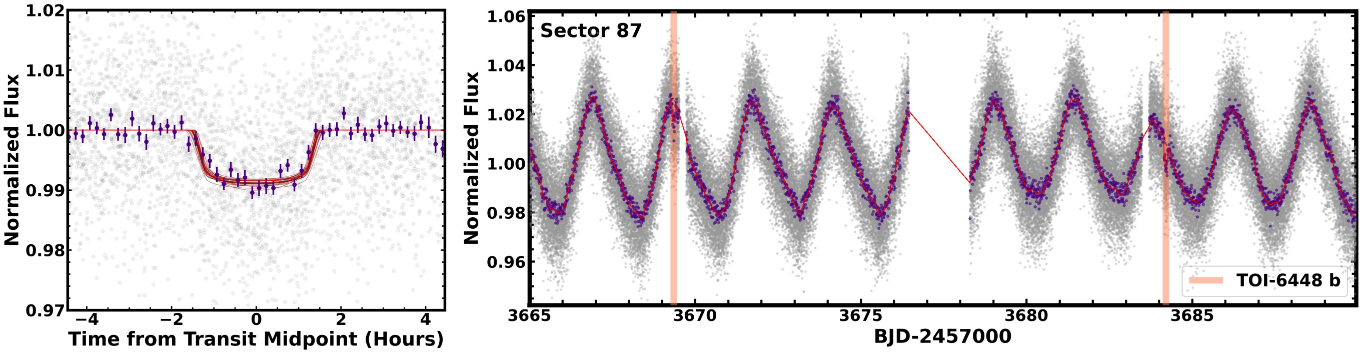

Figure 2. Left: phase-folded TESS light curve of TOI-6448 (gray) binned to 10-minute intervals (purple) for clarity. The best-fit transit model is shown as the bright, opaque red line, with 25 sample fits pulled from the posterior shown as the dark, translucent red lines. The GP has been removed from the data and model. Right: representative section of the TESS light curve (gray) binned to 10-minute intervals (purple) for clarity. The red line shows the GP model, and the pink lines show the locations of the transit events.

Table 4
TESS Transit Parameters of TOI-6448b

Description	Parameter	Value	
		e-float (preferred)	$e = 0$
Measured Planet Parameters			
Time of inferior conjunction	T_0 (BJD −2,457,000)	2214.6125 ± 0.0026	$2214.6127^{+0.0025}_{-0.0024}$
Orbital period	P (days)	$14.844281^{+3.1\times10^{-5}}_{-3.4\times10^{-5}}$	$14.844281^{+3\times10^{-5}}_{-3.2\times10^{-5}}$
Planet-to-star radius ratio	$R_P/R_\star$	$0.0896^{+0.0049}_{-0.005}$	$0.088^{+0.0044}_{-0.0043}$
Impact parameter	b	$0.09^{+0.55}_{-0.7}$	$-0.02^{+0.5}_{-0.48}$
Eccentricity parameter	$\sqrt{e}\sin\omega$	$0.15^{+0.19}_{-0.23}$	…
Eccentricity parameter	$\sqrt{e}\cos\omega$	$-0.01^{+0.44}_{-0.49}$	…
Stellar Parameters			
Stellar density	$\rho_\star$ ($\rho_\odot$)	$1.48^{+0.35}_{-0.36}$	$3.61^{+0.89}_{-1.0}$
Limb-darkening coefficient	q_1	$0.43^{+0.34}_{-0.27}$	$0.43^{+0.34}_{-0.25}$
Limb-darkening coefficient	q_2	$0.24^{+0.17}_{-0.16}$	0.24 ± 0.16
GP Parameters			
Standard deviation	σ	$0.0713^{+0.0048}_{-0.0039}$	$0.0713^{+0.0048}_{-0.004}$
Period	P (days)	$2.662^{+0.078}_{-0.073}$	$2.666^{+0.077}_{-0.073}$
Damping timescale	τ (days)	$2.9^{+0.35}_{-0.18}$	$2.89^{+0.33}_{-0.18}$
Derived Parameters			
Semimajor-axis-to-stellar-radius ratio	$a/R_\star$	$31.7^{+2.7}_{-3.1}$	$39.0^{+3.0}_{-5.5}$
Inclination	i (deg)	$89.8^{+1.4}_{-1.1}$	$90.02^{+0.75}_{-0.77}$
Transit duration (first to fourth contact)	T_{14} (days)	$0.139^{+0.052}_{-0.026}$	$0.1247^{+0.0058}_{-0.0047}$
Planet radius	R_P (R_J)	$0.782^{+0.074}_{-0.075}$	0.768 ± 0.071
	R_P ($R_\oplus$)	$8.77^{+0.83}_{-0.84}$	8.61 ± 0.80
Semimajor axis	a (au)	$0.132^{+0.015}_{-0.017}$	$0.163^{+0.018}_{-0.026}$
Equilibrium temperature[a]	$T_{\rm eq}$ (K)	$742.0^{+38.0}_{-33.0}$	$669.0^{+49.0}_{-27.0}$
Eccentricity	e	$0.2^{+0.21}_{-0.12}$	…
Argument of periastron	ω (deg)	$127.0^{+76.0}_{-97.0}$	…

Note.
[a] Assuming zero albedo.

We ran the MCMC with 50 walkers for 100,000 steps and a 20% burn-in. We present the best-fit parameters in Table 6. While the ground-based data are relatively precise, there are far more TESS data, and the ground-based data did not significantly improve the baseline (which would normally provide significant improvements in P). Thus, we find only a slight improvement to the T_0, period, and R_P/R_* parameters compared to the TESS-only fit.

Table 5
Ground-based Transit Parameters of TOI-6448b

Description	Parameter	Value			
		R_c	$I + z$	g'	
Planet Parameters					
Planet-to-star radius ratio	$R_P/R_\star$	$0.0829^{+0.0040}_{-0.0041}$	0.0866 ± 0.0022	$0.0818^{+0.0047}_{-0.0045}$	
Time of inferior conjunction	T_0 (BJD –2,457,000)	$3357.62350^{+0.00079}_{-0.00084}$		$3639.6568^{+0.0029}_{-0.0028}$	3654.5041 ± 0.0012
Variability Parameters					
Constant	a	-0.00685 ± 0.00085	0.00218 ± 0.00040	-0.0030 ± 0.0010	-0.00639 ± 0.00065
Linear coefficient	b	0.059 ± 0.025	-0.033 ± 0.011	0.156 ± 0.065	0.131 ± 0.026
Quadratic coefficient	c	-0.17 ± 0.12	0.117 ± 0.055	-0.54 ± 0.72	-0.11 ± 0.14

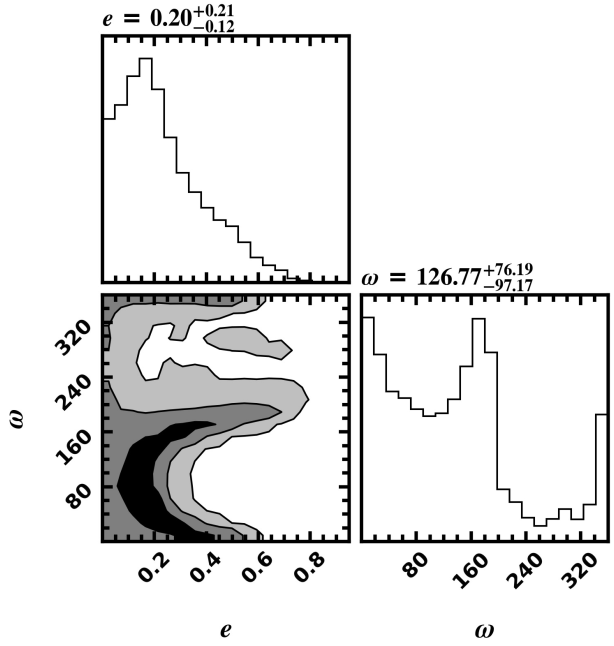

Figure 3. Corner plot of the eccentricity (e) and argument of periastron (ω) fit from the TESS data. Though the eccentric fit is preferred, the (e) posterior agrees with a circular orbit.

Table 6
Global Transit Parameters of TOI-6448 b

Description	Parameter	Value
Measured Planet Parameters		
Time of inferior conjunction	T_0 (BJD – 2,457,000)	$2214.6136^{+0.0024}_{-0.0023}$
Orbital period	P (days)	$14.844261^{+2.7\times10^{-5}}_{-2.8\times10^{-5}}$
Planet-to-star radius ratio	$R_P/R_\star$	0.0866 ± 0.0038
Impact parameter	b	$0.51^{+0.14}_{-0.95}$
Eccentricity parameter	$\sqrt{e}\,\sin\omega$	$0.14^{+0.17}_{-0.23}$
Eccentricity parameter	$\sqrt{e}\,\cos\omega$	$-0.17^{+0.54}_{-0.47}$
Stellar Parameters		
Stellar density	$\rho_\star$ ($\rho_\odot$)	$1.48^{+0.36}_{-0.37}$
TESS limb-darkening coefficient	$q_{1,\mathrm{TESS}}$	$0.452^{+0.094}_{-0.092}$
TESS limb-darkening coefficient	$q_{2,\mathrm{TESS}}$	$0.219^{+0.098}_{-0.090}$
g' limb-darkening coefficient	$q_{1,g'}$	$0.931^{+0.047}_{-0.071}$
g' limb-darkening coefficient	$q_{2,g'}$	$0.265^{+0.093}_{-0.091}$
$I + z$ limb-darkening coefficient	$q_{1,I+z}$	0.597 ± 0.094
$I + z$ limb-darkening coefficient	$q_{2,I+z}$	$0.255^{+0.091}_{-0.097}$
GP Parameters		
Standard deviation	σ	$0.0699^{+0.0045}_{-0.0037}$
Period	P (days)	$2.649^{+0.078}_{-0.070}$
Damping timescale	τ (days)	$2.83^{+0.29}_{-0.16}$
Derived Parameters		
Semimajor-axis-to-stellar-radius ratio	$a/R_\star$	$31.5^{+2.4}_{-2.1}$
Inclination	i (deg)	$88.95^{+1.96}_{-0.34}$
Transit duration (first to fourth contact)	T_{14} (days)	$0.147^{+0.073}_{-0.028}$
Planet radius	R_P (R_J)	0.756 ± 0.068
	R_P ($R_\oplus$)	8.47 ± 0.76
Semimajor axis	a (au)	0.131 ± 0.014
Equilibrium temperature[a]	T_eq (K)	$745.0^{+28.0}_{-31.0}$
Eccentricity	e	$0.2^{+0.26}_{-0.12}$
Argument of periastron	ω (deg)	$143.9^{+52.1}_{-100.0}$

Note.
[a] Assuming zero albedo.

5. Injection–Recovery Analysis

We performed an injection–recovery analysis to determine our sensitivity to additional planets in the system and the reliability of the detection of TOI-6448b.

We injected 10,000 randomly generated synthetic planet signals into the raw light curve extracted in Section 2.1. Planets were given a radius of 0.01–12 $R_\oplus$, a period of 0.5–30 days, and T_0 between the start of the first sector and one period away. For simplicity, we restrict eccentricity to 0. We then reran `Notch` to attempt to recover the signal. A signal is considered "recovered" if `Notch` identifies the correct planet period and T_0 (allowing for a 1% deviation from the input on either) at $\geqslant 8\sigma$ significance. We show the resulting distribution in Figure 5. TOI-6448b lands in a region with ~80% recoverability.

6. False-positive Analysis

Using `TRICERATOPS` (S. Giacalone & C. D. Dressing 2020), we initially calculated a false-positive probability (FPP) $\sim$ 12%. `TRICERATOPS` favored TIC 320411046 as the source of a nearby eclipsing binary (NEB) scenario. The ground-based transits exclude this source (separation $\simeq 25''$),

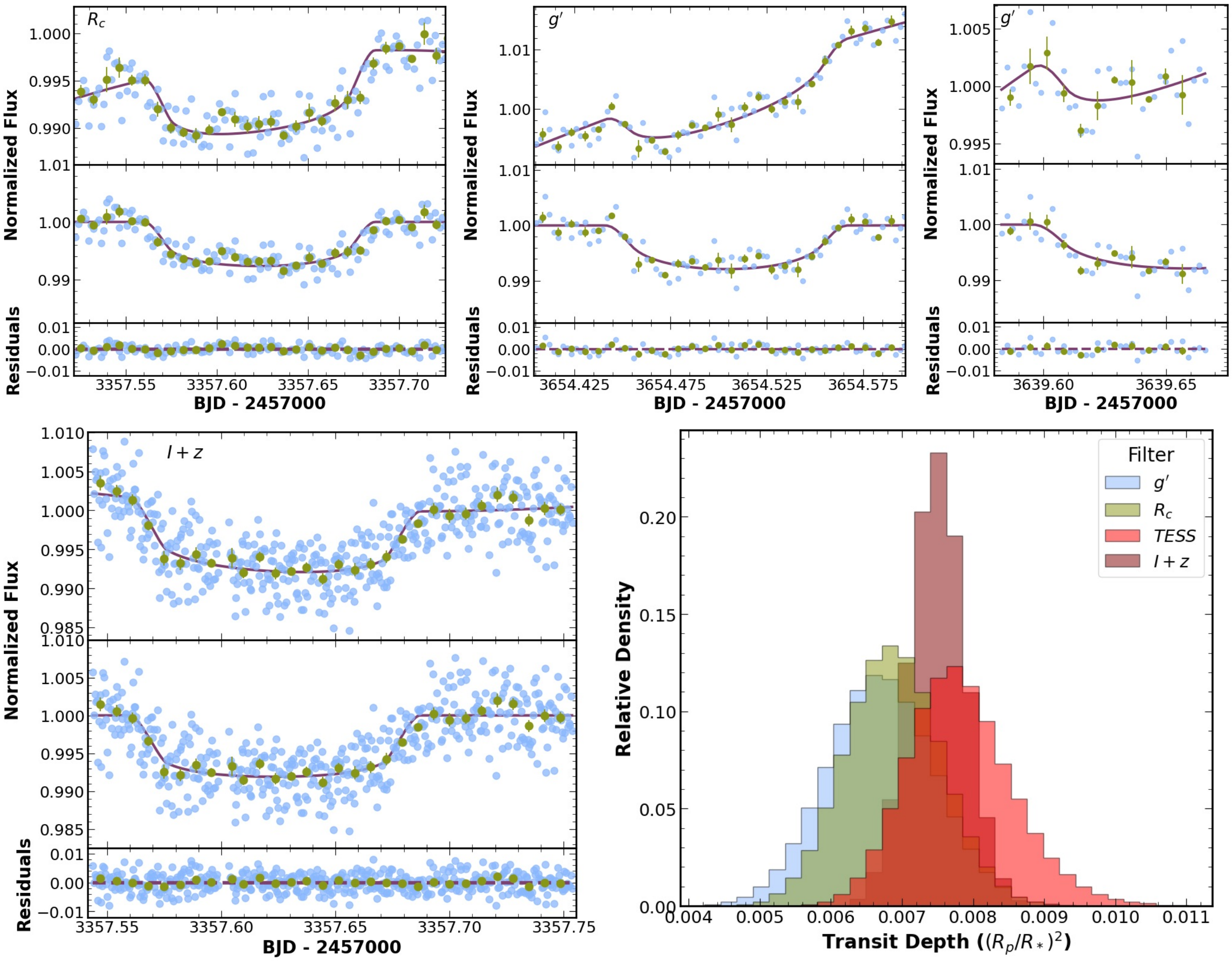

Figure 4. Ground-based light curves (blue) binned to 10-minute intervals (green) for clarity. The transit model is shown in purple. In each set, the upper panel is the raw data, the middle panel has the stellar variability model removed, and the lower panel is the residuals. Bottom right: transit depth, measured by $(R_p/R_*)^2$, posterior from each transit fit.

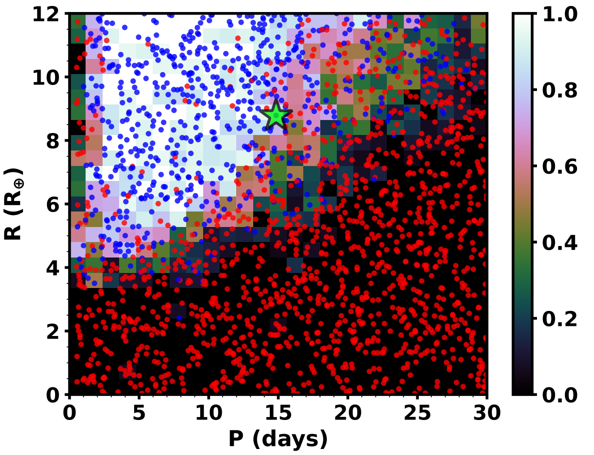

Figure 5. Injection–recovery map in period–radius space for TOI-6448. The green star marks TOI-6448b. Blue circles indicate recovered planets, and red circles are planets that were not recovered. Only 20% of the individual injected signals are shown for clarity. The background is color-coded by overall completeness for a given bin.

ruling out this scenario (see Section 2.2.1 and text below). Recalculating the FPP with this NEB excluded, we find an FPP $< 10^{-5}$, statistically validating the signal as a transiting planet orbiting TOI-6448.

A typical statistical false-positive assessment (such as with `TRICERATOPS`) for young planets can be complicated by young stellar morphology and the puffy planet size. Large ($5-12\ R_\oplus$) planets are rare around old stars but common around <200 Myr systems (e.g., R. B. Fernandes et al. 2022; S. Vach et al. 2024), so the priors will significantly overestimate the FPP. Further, `TRICERATOPS` and similar codes require detrended data, and the results on highly variable stars are sensitive to the quality of the detrending. So we also statistically validate the planet using the combination of follow-up data and the overall properties of the light curve. We handle the potential sources of false positives one at a time below.

Stellar variations. the transit depth is consistent over 4 yr and across the four wavelengths to $<1\sigma$ (TESS, g', R_c, and $I + z$). This excludes stellar signals like spots or flares that change over these timelines and with wavelength.

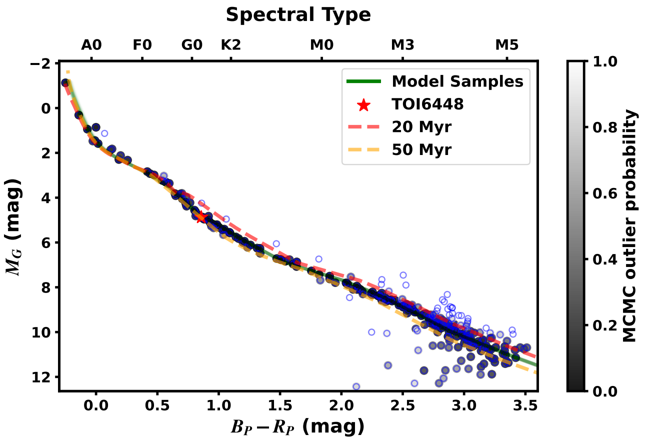

Figure 6. CMD of stars <35 pc and tangential velocity <1 km s^{-1} away from TOI-6448 (blue circles) compared to model predictions from PARSEC. Each target is shaded based on the probability that it is part of the single-star single-age population. Green lines show 100 random samples from the MCMC, and an older model (orange dashed) and a younger model (red dashed) are shown for comparison. The age is tightly constrained by the handful of BA stars, the pre-main-sequence M dwarfs, and the lack of pre-main-sequence G dwarfs. Many of the stars above the sequence are consistent with being binaries, while many below the sequence are likely nonmembers or stars with low-SNR Gaia$_{\mathrm{Bp}}$ photometry.

An eclipsing system orbiting TOI-6448. An eclipsing system should show V-shaped transits, particularly at redder bands where the contrast ratio is more favorable. More importantly, at 35 Myr, a brown dwarf or low-mass star will be pre-main-sequence and have a radius of $>15\ R_\oplus$ (M. S. Marley et al. 2021). Such a star would emit negligible flux compared to the primary in our bluest filter (so the inferred depth is reflective of the size of the eclipsing object). Our transit fit is 7σ below this.

An unseen star (bound or background). The last possible scenario is that the transit signal is associated with another star, either a bound or unassociated eclipsing or transiting system. We can provide a range of constraints on any unseen object from the transit, spectra, and archival imaging.

The transit shape and depth set the magnitude limit for the faintest companion that could cause the transit. Following A. Vanderburg et al. (2019), we find that the companion would need to be $\Delta T < 1.92$ mag at 95% confidence.

We can also set color limits on any possible companion using the transit depths from the four wavelengths (B. M. Tofflemire et al. 2021). A stellar companion would cause the transit depth to vary across wavelength as the companion's relative contribution changes with wavelength. Using the 95th percentile of the distribution of the transit depth ratio, we find that the $T - I + z$ color sets the tightest limit, requiring the companion to be <0.2 mag redder than the primary.

The transit is recovered in ground-based imaging with apertures as small as $3\farcs7$. This easily excludes the main source of false positives from `TRICERATOPS`. No source is detected in Gaia imaging within that region, which can detect stars down to $G \simeq 20$ within $0\farcs8$ of the primary (C. Ziegler et al. 2018). Gaia is sensitive to any star that satisfies the color and magnitude constraints above; the only remaining option is for a source that is unresolved in Gaia.

We can set limits on the brightness of any unresolved star using the population's color–magnitude diagram (CMD; see Figure 6). In a well-populated CMD of single stars with a common age, stars of a given color occupy a narrow locus with a measured vertical scatter σ_M in absolute magnitude. Any unresolved companion adds flux to the combined system, and the contrast between the primary and companion (Δm) satisfies

$$\Delta m \geqslant -2.5 \log_{10}[10^{\Delta_{M,\mathrm{lim}}/2.5} - 1], \tag{2}$$

where $\Delta_{M,\mathrm{lim}}$ is the maximum difference between the predicted absolute magnitude and the observed one, accounting for measurement uncertainties and intrinsic scatter in the CMD. Effectively, any unseen companion with a lower contrast than Δm would be detected as a higher-than-expected CMD position.

The offset $\Delta_{M,\mathrm{lim}}$ can be estimated using a model isochrone, but that is subject to systematics in the model. Instead, we use similar stars (within 1 mag in M_G) within the same population, cutting out those with RUWE > 1.2 (likely binaries). This will be conservative, as the sample will contain some real binaries. We then perturb individual star M_G and $B_P - R_P$ colors according to their photometric and parallax uncertainties, and we interpolate their perturbed colors to predict TOI-6448's M_G given its (perturbed) color. We take the 99th percentile limit as $\Delta_{M,\mathrm{lim}}$, which yields a corresponding contrast of $\Delta G > 2.4$ for the unseen companion. This limit is high in part because TOI-6448 sits slightly below the sequence of nearby stars (Figure 6). No bound star is consistent with both the color and brightness limits from the CMD, transit shape, and chromaticity.

The final test is the lack of a second set of lines in our follow-up spectra. Using the SNR of the reddest order of our MIKE spectra, we expect to detect a second set of lines as faint as Δm of 5.82 within $1''$ of the source (the slit size), although this assumes similar-strength spectral features to the primary, low rotational broadening and a velocity offset from the target. Under this false-positive scenario, the background star must also be an eclipsing system, so it should undergo velocity variations that would be likely to appear in the CHIRON spectrum. However, since the parameters of the hypothetical unbound star are unknown, this constraint is only suggestive and is not included in the `MOLUSC` analysis below or the `TRICERATOPS` analysis above.

To help quantify this effect, we use Multi-Observational Limits on Unseen Stellar Companions (MOLUSC; M. L. Wood et al. 2021), which generates synthetic binaries and compares them to observational data. We generated 100,000 synthetic companions to compare to observed RVs and Gaia imaging. We simulate the finite aperture of the ground-based data by adding a contrast curve that is infinite past $3''$. Of the generated synthetic companions, `MOLUSC` ruled out 78.05%. Applying the above TESS magnitude cut based on the transit shape and color cut based on the chromaticity of the transit removes an additional 21.62%. The remaining 335 (0.33%) binaries are all unresolved SB2 with high mass ratios (>0.7) on long-period orbits (>88 yr) that might have velocities similar to the primary. Because the survivors are relatively bright, all 335 are eliminated by the CMD constraints.

The input velocities are from two different instruments, raising the possibility of offsets, but instrumental offsets are generally <100 m s^{-1} (D. Katz et al. 2019), which is small compared to the precision here. Further, brown dwarfs or other close-in systems that would be ruled out by RVs are disfavored owing to the lack of chromaticity, the transit shape, and the predicted transit depth from a 34 Myr brown dwarf. Rerunning

Table 7
Candidate Comoving Stars

Gaia DR3	α (deg, J2016)	δ (deg, J2016)	Gmag (mag)	$B_p - R_p$ (mag)	$V_{\rm off}$ (km $\rm s^{-1}$)	$\rm RV_{exp}$[a] (km $\rm s^{-1}$)	RV[b] (km $\rm s^{-1}$)	$\sigma_{\rm RV}$[b] (km $\rm s^{-1}$)	$P_{\rm rot}$ (days)	$\sigma_{\rm Prot}$ (days)	Vela[c]
5590921485126584832	110.1704	−33.9223	12.77	0.86	0.0	19.1	19.1	2.06	2.41	0.04	Y
5604855080592114048	109.6015	−31.8131	18.93	3.23	0.03	19.54	⋯	⋯	12.41	0.88	N
5592834467864569472	111.2801	−31.9203	17.66	2.83	0.07	19.17	⋯	⋯	13.57	1.05	Y
5592608071548308864	111.936	−32.3345	10.26	0.26	0.07	18.96	10.53	2.95	0.24	0.001	Y
5591821504113055104	114.1769	−33.7603	19.56	2.94	0.1	18.25	⋯	⋯	⋯	⋯	N
5589656088982368768	111.0502	−36.0676	15.47	2.33	0.11	18.56	−0.82	13.54	0.602	0.003	Y
5592540245416913664	111.9919	−32.825	17.90	2.78	0.13	18.88	⋯	⋯	20.0	2.27	N
5592861749497777664	110.585	−32.0637	16.24	2.25	0.13	19.3	⋯	⋯	0.213	0.001	Y
5591628269248524160	111.5287	−33.9179	17.50	2.92	0.14	18.81	⋯	⋯	13.09	0.98	N
5592880235037738496	111.1338	−31.8034	16.85	2.58	0.15	19.22	⋯	⋯	7.86	0.36	Y
⋯	⋯	⋯	⋯	⋯	⋯	⋯	⋯	⋯	⋯	⋯	⋯

Notes.

[a] Expected RV for membership.

[b] From Gaia DR3 (Gaia Collaboration et al. 2023).

[c] Identified in Vela Population IV in T. Cantat-Gaudin et al. (2019).

(This table is available in its entirety in machine-readable form in the online article.)

our analysis absent the input RVs does not change any conclusions.

7. TOI-6448's Parent Population

7.1. Selection of Stars Comoving with TOI-6448

We searched for comoving stars with TOI-6448 using `FriendFinder`[21] (B. M. Tofflemire et al. 2021). Using TOI-6448's RV, `FriendFinder` uses Gaia Data Release 3 astrometry to compute the *XYZ* position and *UVW* velocities for nearby stars and looks for stars within set velocity and position bounds.

Since our main goal of identifying comoving stars is to calculate a precise age of the cluster, we want to identify stars with high probabilities of being true members with a focus on creating a "clean" list rather than a complete one. We also want to ensure that we are removing stars that are likely to be parts of other regions of Vela, which may have similar kinematics but not necessarily the same age. To this end, we searched for stars with a tangential velocity within 1 km $\rm s^{-1}$ and a 3D distance within 40 pc of TOI-6448. This resulted in 393 candidate comoving stars. We list the candidate members in Table 7.

7.2. Connection to Vela

T. Cantat-Gaudin et al. (2019) cluster TOI-6448 into Vela Population IV with a 77% membership probability. Of the 393 stars identified by `FriendFinder`, 221 overlap with the T. Cantat-Gaudin et al. (2019) list (see Figure 7). Of these, 84% (185) have a $\geqslant$90% membership probability.

Multiple other studies place TOI-6448 in Collinder 140 (e.g., X. Pang et al. 2022; S. Qin et al. 2023; M. G. J. van Groeningen et al. 2023), with membership probabilities of 90%–100%. However, T. Cantat-Gaudin et al. (2019) argue that Collinder 140 is part of Vela Population IV, so these studies are all consistent with membership. We will refer to the parent cluster as Vela for the rest of this work.

As we show below, TOI-6448 has rotation consistent with the parent population, which itself is consistent with a $<$80 Myr population. From our CHIRON and MIKE spectra, we estimate a lithium equivalent width of 170 ± 15 mÅ for TOI-6448. This places it solidly within the 20–50 Myr bin from R. D. Jeffries et al. (2023) and solidly rules out ages $>$100 Myr. As we show below, this is consistent with the age of the parent population (35 Myr). Combined with the already high membership probabilities in the literature, we conclude that TOI-6448 is a member of Vela Population IV.

7.3. Age Analysis

T. Cantat-Gaudin et al. (2019) suggest that Vela Population IV is composed of five previously known clusters: NGC 2547, NGC 2451B, Collinder 135, UBC 7, and Collinder 140. The reported ages of these clusters range from 27 to 170 Myr (W. S. Dias et al. 2002; N. V. Kharchenko et al. 2013; D. Bossini et al. 2019).

Motivated by the age spread and importance of this target for statistical work, we decided to reanalyze the age and confirm TOI-6448's membership in Vela Population IV. To derive the most precise age for TOI-6448 and Vela IV, we combine the results of isochronal modeling, variability-based aging, and gyrochronology.

7.3.1. Isochronal Modeling

We fit the Gaia CMD using a mixture model as described in A. W. Mann et al. (2022). To briefly summarize, we compare the Gaia colors and absolute magnitudes (M_G) to the combination of a single-star single-age sequence derived from a model isochrone and a second outlier population. The outlier population may be made of binaries, nonmembers, targets with poor photometry or parallaxes, or members of other (younger or older) regions of Vela. In principle, one could model this using three to five populations in the mixture model instead of just two, e.g., one model targeting member binaries, one capturing field interlopers, another for young Vela interlopers, and a final one for targets with bad measurements. In practice, there are too few stars in these groups to constrain the population parameters.

---

[21] https://github.com/adamkraus/Comove

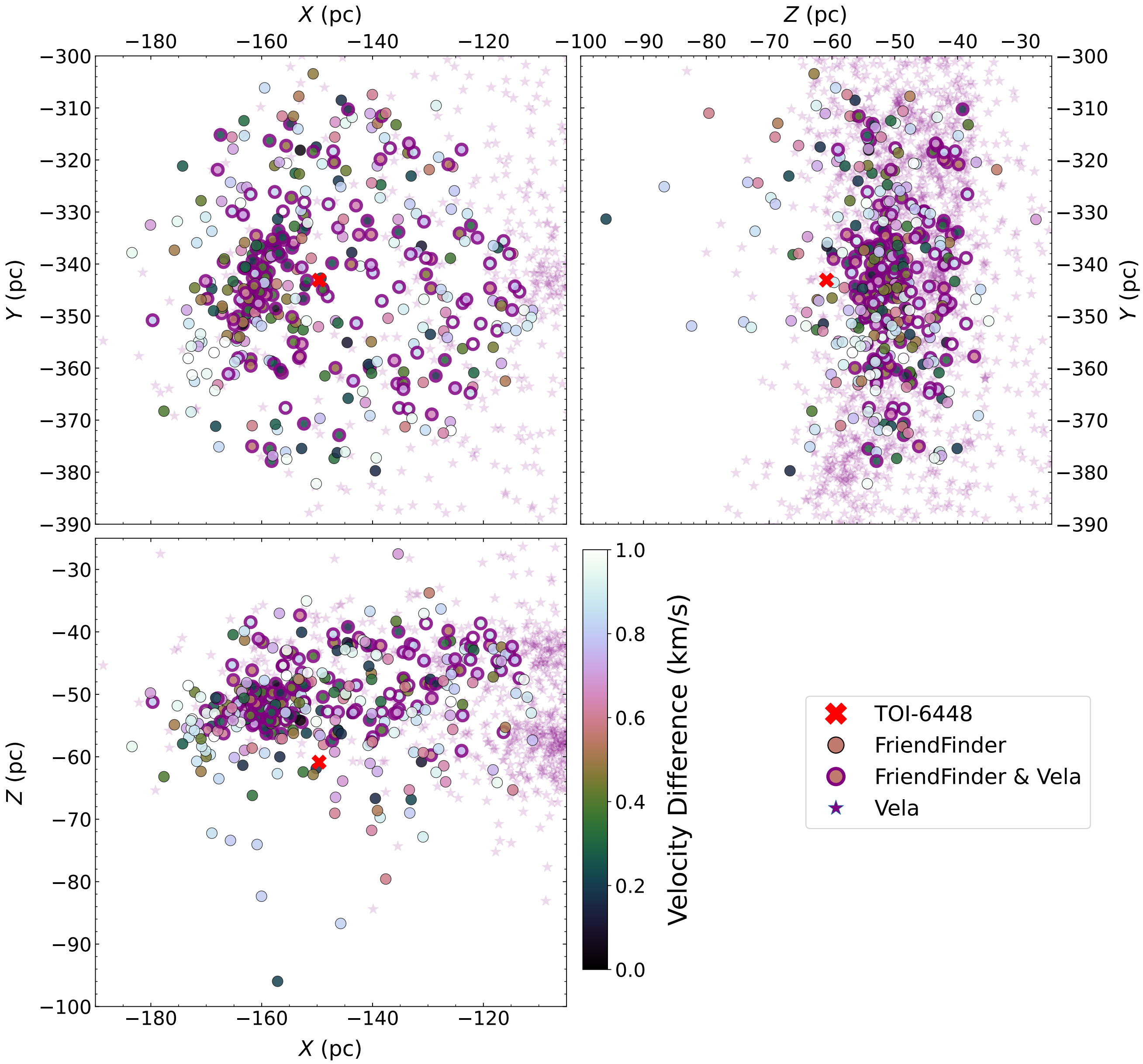

Figure 7. Candidate comoving stars to TOI-6448 (red crosses). All stars identified with `FriendFinder` are shown as the colored circles (colored by their velocity offset to TOI-6448). Stars that are in the same region and identified in T. Cantat-Gaudin et al. (2019) as part of Vela Population IV are shown in the background as the translucent purple stars. Stars that are in both lists are shown as the colored circles outlined in purple.

The main population is modeled using two parameters, the age (τ) and the overall extinction ($E\,(B\,-\,V)$), while the outlier population is modeled as an offset (Y_B) and variance (V_B) from the primary population, both measured in magnitude. Additional parameters f and P_B describe the missing scatter (e.g., differential extinction between stars or underestimated measurement uncertainties) and the amplitude of the outlier population (the fraction of stars not in the single-star single-age group).

We tested models from PARSECv2.0 (C. T. Nguyen et al. 2022) and the Dartmouth Stellar Evolution Program (DSEP; A. Dotter et al. 2008) with magnetic enhancement (DSEP-mag; G. A. Feiden 2016). The results were consistent at $\simeq 2\sigma$, with PARSEC yielding a lower age (31.5 ± 1.5 Myr) than the DSEP-mag models (38 ± 3 Myr). Both fit the overall CMD well, although the DSEP-mag models do not cover the warmest (spectral class B and A) stars in the sample, yielding larger uncertainties.

As can be seen in Figure 6, the age of the population around TOI-6448 is tightly constrained by the handful of BA stars (which evolve quickly), the population of pre-main-sequence M dwarfs, and the lack of pre-main-sequence G and early K dwarfs (which rules out significantly younger ages). The combination also means that the results are weakly sensitive to assumptions about metallicity; adjustments of ±0.2 dex change the age by $\simeq 2$ Myr. Including this and accounting for both grid results, we adopted a more conservative age of 34 ± 3 Myr with a mean reddening of $E\,(B - V) = 0.05 \pm 0.01$.

7.3.2. Variability Age

Taking advantage of variable stars having higher photometric uncertainties and the relationship between stellar

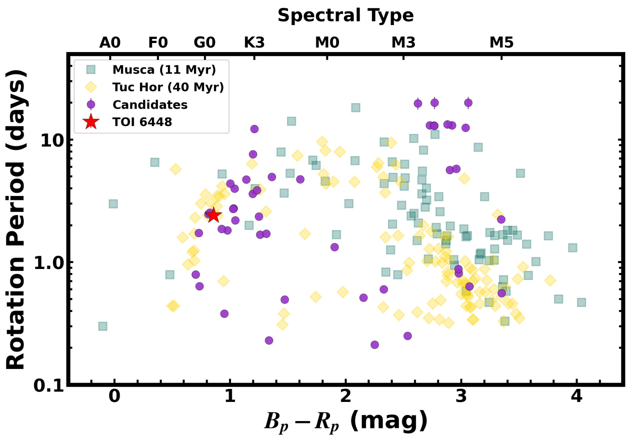

Figure 8. Rotation periods of candidate members (purple circles) comoving with TOI-6448 (red star). Only rotation periods measured to a Lomb–Scargle power >0.03 are shown. The rotation periods for Musca (∼11 Myr; A. W. Mann et al. 2022) and Tuc-Hor (∼40 Myr; J. Gagné et al. 2020; green squares and yellow diamonds, respectively) are shown for reference.

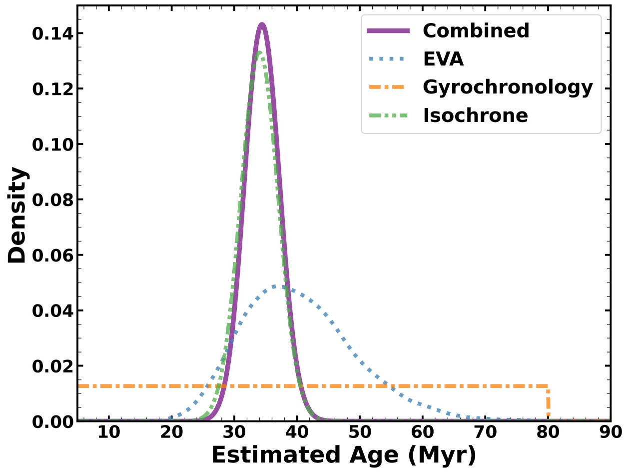

Figure 9. Final age estimate (34 ± 3 Myr; purple) compared to the age estimate from each method (colored lines). The final age is strongly influenced by the isochronal fit, which was far more precise owing to the combination of high-mass evolving stars and pre-main-sequence M dwarfs. However, we highlight that all age metrics agree.

activity and age, M. G. Barber & A. W. Mann (2023) fit a Skumanich-like relationship between age and excess uncertainties in Gaia photometry (M. Riello et al. 2021). We ran Excess Variability-based Age (`EVA`[22]) to query Gaia, make appropriate quality cuts, and compute the age. Using `EVA`, we calculate an age of 39^{+10}_{-8} Myr taking into account all three bands (G, B_P, and R_P), though the ages from the three bands agreed within 1σ with each other.

7.3.3. Gyrochronology

We calculated the rotation periods following M. G. Barber et al. (2025) and A. W. Boyle et al. (2025). To summarize, we downloaded light curves for 298 of the 393 stars in our sample using the `unpopular` package (S. Hattori et al. 2022). Then, for each star and for each sector, we used a Lomb–Scargle periodogram with a linearly spaced search grid with 100,000 steps spanning 0.2–20 days. If a star was observed in multiple sectors, the rotation period corresponding to the highest power was adopted. We assigned uncertainties on the rotation periods using the empirical relation in A. W. Boyle et al. (2025).

We find TOI-6448 to have a rotation period of 2.412 ± 0.037 days. Compared to the remaining candidate members and members of similarly aged young populations (Figure 8), the rotation period of TOI-6448 is consistent with membership.

We attempted to convert the rotation periods to an age estimate using `gyro-interp` (L. G. Bouma et al. 2023). Due to stars spinning up during their first ∼100 Myr, `gyro-interp` is calibrated only for stars >80 Myr. We use the rotation periods to confirm group membership, but gyrochronology only sets an upper limit on the age.

7.3.4. Combining Age Estimates

We determine a final age for TOI-6448 by combining the individual age estimates (Figure 9). Using the likelihood distributions from each method, we find an overall age of 34 ± 3 Myr for TOI-6448 and Vela Population IV. This age is in agreement with previous age determinations, though it provides the much tighter constraint necessary for planet evolution statistical modeling.

8. Discussion and Conclusions

We report the validation of TOI-6448 b, a giant planet orbiting a young Sun-like star. We find TOI-6448 b to be 8.8 ± 0.8 $R_\oplus$ on a 14.844-day orbit. We derive the age of the host star, through the parent association, Vela Population IV, to be 34 ± 3 Myr based on the CMD placements, rotation periods, and variability levels of the stars tightly comoving with TOI-6448.

TOI-6448 b contributes to the growing population of <50 Myr transiting planets that are ideal for understanding the evolutionary pathways that create the mature distribution of planets as discovered by Kepler. There are 10 other <50 Myr systems harboring 16 transiting planets. As can be seen in Figure 10, most of these land in the region of parameter space with few old planets from Kepler (5–11 $R_\oplus$). This is consistent with the small number of mass measurements for these planets that indicate that they are puffy sub-Neptunes or super-Earths (P. C. Thao et al. 2024; S. Barat et al. 2025) and statistical surveys finding enhanced super-Neptune occurrence rates out to at least 200 Myr (S. Vach et al. 2024).

A common concern with this conclusion is the role of observational bias—that the young planet population looks larger because high stellar variability is masking out the smaller planets. Observational bias can explain the deficit of $\lesssim 2\ R_\oplus$ planets in the sample; injection–recovery tests on such stars suggest that we are relatively insensitive to such small planets around <50 Myr stars (e.g., S. Vach et al. 2024). However, it cannot explain why we have detected *an excess* of $>5\ R_\oplus$ planets given the available sample of young stars. The most clear evidence that this is not bias is that stars from 80 to 200 Myr are generally spinning *faster* than their younger counterparts, as they are still spinning up from pre-main-sequence contraction. Indeed, some of the most challenging light curves for planet detection are ≃100 Myr stars (E. Gaidos et al. 2017; A. C. Rizzuto et al. 2017). This slightly older range also contains plenty of stars between Pleiades, α Per, Psc-Eri,

---

[22] https://github.com/madysonb/EVA.

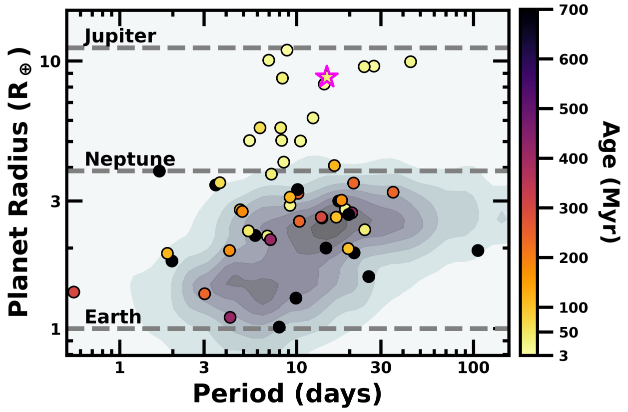

Figure 10. Distribution of planets discovered transiting members of young stellar associations (colored points) compared to the distribution of planets transiting (primarily) mature stars discovered using Kepler (background contours). TOI-6448b is shown as the star outlined in pink. The pale yellow points, representing the youngest population (<50 Myr), tend to sit high in comparison to even slightly older (100–200 Myr) planets.

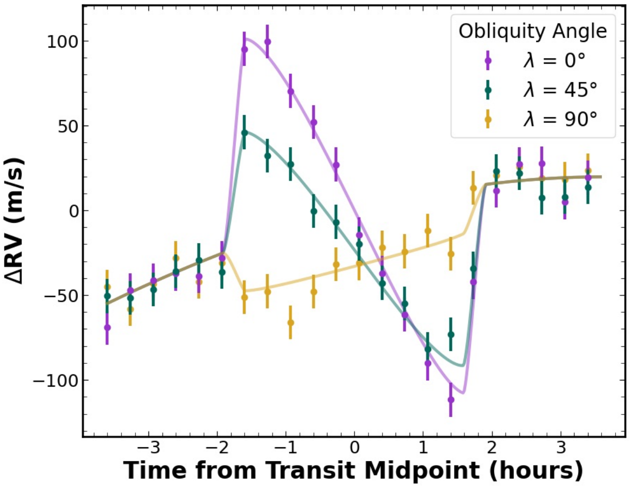

Figure 11. Simulated RM observations for TOI-6448 b for various sky-projected obliquity angles. Even at relatively long cadence (20 minutes), for large uncertainties (10 m s^{-1}), and considering stellar jitter ($\sim$50 m s^{-1} over the transit duration), we can easily distinguish between aligned (purple) and misaligned (green and yellow) orbits.

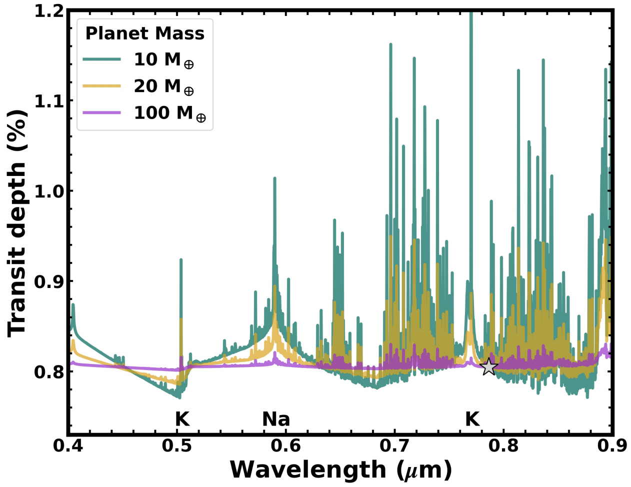

Figure 12. Simulated transmission spectra (R = 15,000) of TOI-6448 b for various planet masses. We label the major lines (Na and K) accessible from ground-based facilities. Each is normalized to the TESS depth at the TESS central wavelength (gray star). We can easily distinguish between a super-Earth progenitor (10 $M_\oplus$; green), a Neptune progenitor (20 $M_\oplus$; yellow), and a Saturn planet (100 $M_\oplus$; purple).

and a number of Theia groups (M. Kounkel et al. 2020). Yet there are far fewer 5–11 $R_\oplus$, 80–200 Myr planets than there are similar-radius, 0–50 Myr planets. Indeed, this sharp drop in the occurrence of 5–11 $R_\oplus$ past $\simeq$50 Myr suggests that the radii of these planets decrease rapidly, as suggested by a "gas dwarf" model (J. G. Rogers 2025).

Counterintuitively, observational bias makes this planet size effect *stronger*. We can show this with a simple simulation. The THYME and TI-DYE surveys have focused on just two regions for <50 Myr stars: Taurus-Auriga and Sco-Cen, with TOI-6448 b as first in our search of Vela-Puppis. Of these three groups, there are 11 planets with periods <30 days and radii of 5–11 $R_\oplus$ that were discovered or recovered by these surveys, all found within a sample of 10,273 stars. If we assume that the surveys are 100% complete to planets in this radius and period range and adopt a Kepler-like planet distribution (star/planet properties from T. A. Berger et al. 2020, 2023), we should detect between one and nine planets (95%). For simplicity, this ignores differences in the target sample, and hence it is marginally consistent with our findings. If we assume that completeness/sensitivity to these younger planets is $\simeq$80% that of Kepler, the expected number of detections becomes zero to seven planets (95%), and the difference becomes $>3\sigma$. The result is similarly significant if we count three candidates that have yet to be validated (e.g., S. Vach et al. 2025) as real (even ignoring completeness).

As can be seen in Figure 5, 80% completeness is likely generous, especially for planets from 15 to 30 days, where it is easy to confuse random stellar signals (flares and rotation) with planetary ones. Younger groups like Upper Scorpius and Taurus-Auriga also have a large population of dipper and burster variable stars (M. Ansdell et al. 2016; A. M. Cody et al. 2017) for which our completeness is $\simeq$0. More importantly, *as we decrease sensitivity to young planets, the difference between young and old planets increases,* the opposite of our standard intuition. For the planet radii to be explained by observational bias, one would need to assume that Kepler is missing the larger planets, despite a larger telescope, longer stare window, and better-behaved stars.

Surveys using Rossiter–McLaughlin (RM) or Doppler tomography (DT) suggest that young planets are more aligned than their older counterparts (e.g., F. Dai et al. 2020; G. Zhou et al. 2020; C. P. Wirth et al. 2021; M. C. Johnson et al. 2022; T. Hirano et al. 2024). However, the samples are still marginally consistent, primarily because the young planet sample is still too small. Young planets are *easier* targets, in part because of their larger radii, but also because the rapid rotation rate of young stars *increases* the RM amplitude. The stellar jitter is also increased, but this tends to work on the multiday timescale of stellar rotation, while RM and DT signals work on the $\sim$hours of the transit duration. As we show in Figure 11, the expected RM signal for TOI-6448 b is hundreds of meters per second for an aligned system, while the jitter of the same time period is expected to be on the order of tens of meters per second.

Assuming that this planet follows the trend of other young planets and predictions from models (J. G. Rogers 2025), it will have a mass of 5–40 $M_\oplus$, resulting in an RV amplitude of just 2–8 m s^{-1}. This is at least 1 order of magnitude below the expected stellar jitter (∼hundreds of meters per second based on the variability). However, prior studies have shown that we can measure the masses of young puffy ($>5\ R_\oplus$) planets from their transmission spectra (e.g., J. de Wit & S. Seager 2013; P. C. Thao et al. 2024; S. Barat et al. 2025). This method is *more* effective at lower masses and works in the presence of strong spots. It is mostly limited by the availability of JWST time.

However, rough masses for these kinds of systems might be possible from the ground. We model expected transmission spectra for TOI-6448 b assuming a super-Earth-progenitor mass ($M = 10\ M_\oplus$), a Neptune-progenitor mass ($M = 20\ M_\oplus$), and a Saturn mass ($M = 100\ M_\oplus$), using the basic parameters from P. C. Thao et al. (2024) and PICASO (N. E. Batalha et al. 2019). We assume a cloudless atmosphere, consistent with the previous JWST observations of HIP 67522b and V1298 Tau b. As we show in Figure 12, these scenarios are distinguishable in the optical at a resolution of $R \simeq 15{,}000$ and a precision of a few millimagnitudes per resolving element; this is routinely achieved using high-precision spectrographs (e.g., S. Benatti et al. 2021; T. Hirano et al. 2024). Since H_2O bands are not accessible from the ground, the analysis relies on Na and K atomic lines in the optical, which are measurable owing to the lower surface gravity. These features are also advantageous because the expected spot temperatures do not produce such lines (P. C. Thao et al. 2023).

Acknowledgments

The authors would like to thank Halee and Bandit for their scientific feedback and reminders (demands) to take writing breaks. M.G.B. and A.W.M. were supported by NASA's exoplanet research program (XRP 80NSSC25K7148), and M. G.B. was also supported by the NSF Graduate Research Fellowship (DGE-2040435). K.A.C. acknowledges support from the TESS mission via subaward s3449 from MIT. Funding for K.B. was provided by the European Union (ERC AdG SUBSTELLAR, GA 101054354). W.C.S. acknowledges funding from the NC Space Grant Undergraduate Research Scholarship and a Summer Undergraduate Research Fellowship from the Office for Undergraduate Research at the University of North Carolina at Chapel Hill.

Funding for the TESS mission is provided by NASA's Science Mission Directorate. We acknowledge the use of public TESS data from pipelines at the TESS Science Office and at the TESS Science Processing Operations Center. Resources supporting this work were provided by the NASA High-End Computing (HEC) Program through the NASA Advanced Supercomputing (NAS) Division at Ames Research Center for the production of the SPOC data products. TESS data presented in this paper were obtained from the Mikulski Archive for Space Telescopes (MAST) at the Space Telescope Science Institute.

This research has made use of the Exoplanet Follow-up Observation Program (ExoFOP; NExScI 2022) website, which is operated by the California Institute of Technology, under contract with the National Aeronautics and Space Administration under the Exoplanet Exploration Program.

This research has used data from the CTIO/SMARTS 1.5 m telescope, which is operated as part of the SMARTS Consortium by RECONS (www.recons.org) members Todd Henry, Hodari James, Wei-Chun Jao, and Leonardo Paredes.

This work has made use of data from the European Space Agency (ESA) mission Gaia (https://www.cosmos.esa.int/gaia), processed by the Gaia Data Processing and Analysis Consortium (DPAC; https://www.cosmos.esa.int/web/gaia/dpac/consortium). Funding for the DPAC has been provided by national institutions, in particular the institutions participating in the Gaia Multilateral Agreement.

This work makes use of observations from the LCOGT network. Part of the LCOGT telescope time was granted by NOIRLab through the Mid-Scale Innovations Program (MSIP). MSIP is funded by NSF.

This paper is based on observations made with the Las Cumbres Observatory's education network telescopes that were upgraded through generous support from the Gordon and Betty Moore Foundation.

The research leading to these results has received funding from the ARC grant for Concerted Research Actions, financed by the Wallonia-Brussels Federation. TRAPPIST is funded by the Belgian Fund for Scientific Research (Fond National de la Recherche Scientifique, FNRS) under the grant PDR T.0120.21. M.G. is F.R.S.-FNRS Research Director.

ORCID iDs

Madyson G. Barber https://orcid.org/0000-0002-8399-472X
Andrew W. Mann https://orcid.org/0000-0003-3654-1602
Andrew Vanderburg https://orcid.org/0000-0001-7246-5438
Khalid Barkaoui https://orcid.org/0000-0003-1464-9276
Karen A. Collins https://orcid.org/0000-0001-6588-9574
Sebastian Carrazco-Gaxiola https://orcid.org/0009-0006-9244-3707
Phil Evans https://orcid.org/0000-0002-5674-2404
Matthew J. Fields https://orcid.org/0000-0002-9641-3138
Michaël Gillon https://orcid.org/0000-0003-1462-7739
Todd J. Henry https://orcid.org/0000-0002-9061-2865
Katharine M. Hesse https://orcid.org/0000-0002-2135-9018
Wei-Chun Jao https://orcid.org/0000-0003-0193-2187
Emmanuel Jehin https://orcid.org/0000-0001-8923-488X
Sydney Jenkins https://orcid.org/0000-0001-9827-1463
Tim Johns https://orcid.org/0009-0006-4398-4654
David R. Rodriguez https://orcid.org/0000-0003-1286-5231
Richard P. Schwarz https://orcid.org/0000-0001-8227-1020
William C. Storch https://orcid.org/0009-0008-5045-1500
Cristilyn N. Watkins https://orcid.org/0000-0001-8621-6731
Francis P. Wilkin https://orcid.org/0000-0003-2127-8952

References

Allard, F., Homeier, D., Freytag, B., et al. 2013, MSAIS, 24, 128
Alves, D. R., Jenkins, J. S., Vines, J. I., et al. 2025, MNRAS, 536, 1538
Ansdell, M., Gaidos, E., Rappaport, S. A., et al. 2016, ApJ, 816, 69
Barat, S., Désert, J.-M., Goyal, J. M., et al. 2024, A&A, 692, A198
Barat, S., Désert, J.-M., Mukherjee, S., et al. 2025, AJ, 170, 165
Barber, M. G., & Mann, A. W. 2023, ApJ, 953, 127
Barber, M. G., Mann, A. W., Vanderburg, A., Boyle, A. W., & Lopez Murillo, A. I. 2025, AJ, 170, 32
Barber, M. G., Mann, A. W., Vanderburg, A., et al. 2024a, Natur, 635, 574

Barber, M. G., Thao, P. C., Mann, A. W., et al. 2024b, ApJL, 973, L30

Batalha, N. E., Marley, M. S., Lewis, N. K., & Fortney, J. J. 2019, ApJ, 878, 70

Benatti, S., Damasso, M., Borsa, F., et al. 2021, A&A, 650, A66

Berger, T. A., Huber, D., Gaidos, E., van Saders, J. L., & Weiss, L. M. 2020, AJ, 160, 108

Berger, T. A., Schlieder, J. E., & Huber, D. 2023, arXiv:2301.11338

Bernstein, R., Shectman, S. A., Gunnels, S. M., Mochnacki, S., Athey, A. E., et al. 2003, Proc. SPIE, 4841, 1694

Blackwell, D. E., & Shallis, M. J. 1977, MNRAS, 180, 177

Blunt, S., Carvalho, A., David, T. J., et al. 2023, AJ, 166, 62

Bossini, D., Vallenari, A., Bragaglia, A., et al. 2019, A&A, 623, A108

Bouma, L. G., Kerr, R., Curtis, J. L., et al. 2022, AJ, 164, 215

Bouma, L. G., Palumbo, E. K., & Hillenbrand, L. A. 2023, ApJL, 947, L3

Boyle, A. W., Mann, A. W., Bush, J., et al. 2025, ApJ, 985, 233

Bressan, A., Marigo, P., Girardi, L., et al. 2012, MNRAS, 427, 127

Brown, T. M., Baliber, N., Bianco, F. B., et al. 2013, PASP, 125, 1031

Burn, R., Mordasini, C., Mishra, L., et al. 2024, NatAs, 8, 463

Cantat-Gaudin, T., Jordi, C., Wright, N. J., et al. 2019, A&A, 626, A17

Capistrant, B. K., Soares-Furtado, M., Vanderburg, A., et al. 2024, AJ, 167, 54

Cody, A. M., Hillenbrand, L. A., David, T. J., et al. 2017, ApJ, 836, 41

Collins, K. 2019, AAS Meeting, 233, 140.05

Collins, K. A., Kielkopf, J. F., Stassun, K. G., & Hessman, F. V. 2017, AJ, 153, 77

Cutri, R. M., Wright, E. L., Conrow, T., et al. 2014, yCat, 2328, 0

Dai, F., Goldberg, M., Batygin, K., et al. 2024, AJ, 168, 239

Dai, F., Roy, A., Fulton, B., et al. 2020, AJ, 160, 193

David, T. J., Cody, A. M., Hedges, C. L., et al. 2019a, AJ, 158, 79

David, T. J., Petigura, E. A., Luger, R., et al. 2019b, ApJL, 885, L12

de Wit, J., & Seager, S. 2013, Sci, 342, 1473

Dias, W. S., Alessi, B. S., Moitinho, A., & Lépine, J. R. D. 2002, A&A, 389, 871

Dotter, A., Chaboyer, B., Jevremović, D., et al. 2008, ApJS, 178, 89

Evans, D. W., Riello, M., De Angeli, F., et al. 2018, A&A, 616, A4

Feiden, G. A. 2016, A&A, 593, A99

Fernandes, R. B., Mulders, G. D., Pascucci, I., et al. 2022, AJ, 164, 78

Fields, M. J., Mann, A. W., Kesseli, A., & Boyle, A. W. 2025, RASTI, 4, 17

Foreman-Mackey, D. 2018, RNAAS, 2, 31

Foreman-Mackey, D., Agol, E., Ambikasaran, S., & Angus, R. 2017, AJ, 154, 220

Foreman-Mackey, D., Hogg, D. W., Lang, D., & Goodman, J. 2013, PASP, 125, 306

Gagné, J., David, T. J., Mamajek, E. E., et al. 2020, ApJ, 903, 96

Gaia Collaboration, Vallenari, A., Brown, A. G. A., et al. 2023, A&A, 674, A1

Gaidos, E., Mann, A. W., Lépine, S., et al. 2014, MNRAS, 443, 2561

Gaidos, E., Mann, A. W., Rizzuto, A., et al. 2017, MNRAS, 464, 850

Giacalone, S., & Dressing, C. D., 2020 triceratops: Candidate Exoplanet Rating Tool, Astrophysics Source Code Library, ascl:2002.004

Gilbert, E. A., Barclay, T., Quintana, E. V., et al. 2022, AJ, 163, 147

Gillon, M., Jehin, E., Magain, P., et al. 2011, EPJWC, 11, 06002

Ginzburg, S., Schlichting, H. E., & Sari, R. 2016, ApJ, 825, 29

Goodman, J., & Weare, J. 2010, Commun. Appl. Math. Comput. Sci., 5, 65

Hattori, S., Foreman-Mackey, D., Hogg, D. W., et al. 2022, AJ, 163, 284

Heap, S. R., & Lindler, D. J. 2007, ASPC, 374, 409

Henden, A. A., Levine, S. E., Terrell, D., Smith, T. C., & Welch, D. 2012, JAVSO, 40, 430

Hirano, T., Gaidos, E., Harakawa, H., et al. 2024, MNRAS, 530, 3117

Husser, T.-O., Wende-von Berg, S., Dreizler, S., et al. 2013, A&A, 553, A6

Jeffries, R. D., Jackson, R. J., Wright, N. J., et al. 2023, MNRAS, 523, 802

Jehin, E., Gillon, M., Queloz, D., et al. 2011, Msngr, 145, 2

Johnson, M. C., Dai, F., Justesen, A. B., et al. 2018, MNRAS, 481, 596

Johnson, M. C., David, T. J., Petigura, E. A., et al. 2022, AJ, 163, 247

Karalis, A., Lee, E. J., & Thorngren, D. P. 2025, ApJ, 978, 46

Katz, D., Sartoretti, P., Cropper, M., et al. 2019, A&A, 622, A205

Kelson, D. D. 2003, PASP, 115, 688

Kelson, D. D., Illingworth, G. D., van Dokkum, P. G., & Franx, M. 2000, ApJ, 531, 159

Kenyon, S. J., & Hartmann, L. 1995, ApJS, 101, 117

Kesseli, A. Y., Muirhead, P. S., Mann, A. W., & Mace, G. 2018, AJ, 155, 225

Kharchenko, N. V., Piskunov, A. E., Schilbach, E., Röser, S., & Scholz, R.-D. 2013, A&A, 558, A53

Kipping, D. M. 2013, MNRAS, 435, 2152

Koepferl, C. M., Ercolano, B., Dale, J., et al. 2013, MNRAS, 428, 3327

Kounkel, M., Covey, K., & Stassun, K. G. 2020, AJ, 160, 279

Kreidberg, L. 2015, PASP, 127, 1161

Kunimoto, M., Daylan, T., Guerrero, N., et al. 2022, ApJS, 259, 33

Lee, E. J., Chiang, E., & Ormel, C. W. 2014, ApJ, 797, 95

Luque, R., & Pallé, E. 2022, Sci, 377, 1211

Mann, A. W., Gaidos, E., & Ansdell, M. 2013, ApJ, 779, 188

Mann, A. W., Gaidos, E., Mace, G. N., et al. 2016a, ApJ, 818, 46

Mann, A. W., Newton, E. R., Rizzuto, A. C., et al. 2016b, AJ, 152, 61

Mann, A. W., Wood, M. L., Schmidt, S. P., et al. 2022, AJ, 163, 156

Marimbu, K., & Lee, E. J. 2024, RNAAS, 8, 208

Marley, M. S., Saumon, D., Visscher, C., et al. 2021, ApJ, 920, 85

Masuda, K., & Winn, J. N. 2020, AJ, 159, 81

McCully, C., Volgenau, N. H., Harbeck, D.-R., et al. 2018, Proc. SPIE, 10707, 107070K

Mordasini, C., Alibert, Y., & Benz, W. 2009, A&A, 501, 1139

NExScI 2022, Exoplanet Follow-up Observing Program Web Service, IPAC, doi:10.26134/EXOFOP5

Nguyen, C. T., Costa, G., Girardi, L., et al. 2022, A&A, 665, A126

Pang, X., Tang, S.-Y., Li, Y., et al. 2022, ApJ, 931, 156

Paredes, L. A., Henry, T. J., Quinn, S. N., et al. 2021, AJ, 162, 176

Parviainen, H., & Aigrain, S. 2015, MNRAS, 453, 3821

Qin, S., Zhong, J., Tang, T., & Chen, L. 2023, ApJS, 265, 12

Rayner, J. T., Cushing, M. C., & Vacca, W. D. 2009, ApJS, 185, 289

Riello, M., De Angeli, F., Evans, D. W., et al. 2021, A&A, 649, A3

Rizzuto, A. C., Mann, A. W., Vanderburg, A., Kraus, A. L., & Covey, K. R. 2017, AJ, 154, 224

Rizzuto, A. C., Newton, E. R., Mann, A. W., et al. 2020, AJ, 160, 33

Rogers, J. G. 2025, MNRAS, 539, 2230

Rogers, J. G., Owen, J. E., & Schlichting, H. E. 2024, MNRAS, 529, 2716

Skrutskie, M. F., Cutri, R. M., Stiening, R., et al. 2006, AJ, 131, 1163

Tayar, J., Claytor, Z. R., Huber, D., & van Saders, J. 2022, ApJ, 927, 31

TESS Team 2021, TESS "Fast" Light Curves—All Sectors, STScI/MAST, doi:10.17909/T9-ST5G-3177

TESS Team 2022, TESS Raw Full Frame Images: All Sectors, STScI/MAST, doi:10.17909/3Y7C-WA45

Thao, P. C., Mann, A. W., Barber, M. G., et al. 2024, AJ, 168, 41

Thao, P. C., Mann, A. W., Feinstein, A. D., et al. 2024, AJ, 168, 297

Thao, P. C., Mann, A. W., Gao, P., et al. 2023, AJ, 165, 23

Tofflemire, B. M., Rizzuto, A. C., Newton, E. R., et al. 2021, AJ, 161, 171

Tokovinin, A., Fischer, D. A., Bonati, M., et al. 2013, PASP, 125, 1336

Vach, S., Zhou, G., Huang, C. X., et al. 2024, AJ, 167, 210

Vach, S., Zhou, G., Mann, A. W., et al. 2025, AJ, 170, 131

Van Eylen, V., & Albrecht, S. 2015, ApJ, 808, 126

van Groeningen, M. G. J., Castro-Ginard, A., Brown, A. G. A., Casamiquela, L., & Jordi, C. 2023, A&A, 675, A68

Vanderburg, A., Huang, C. X., Rodriguez, J. E., et al. 2019, ApJL, 881, L19

Venturini, J., Alibert, Y., & Benz, W. 2016, A&A, 596, A90

Villaume, A., Conroy, C., Johnson, B., et al. 2017, ApJS, 230, 23

Weisserman, D., Becker, J. C., & Vanderburg, A. 2023, AJ, 165, 89

Wirth, C. P., Zhou, G., Quinn, S. N., et al. 2021, ApJL, 917, L34

Wolf, C., Onken, C. A., Luvaul, L. C., et al. 2018, PASA, 35, e010

Wolfgang, A., Rogers, L. A., & Ford, E. B. 2016, ApJ, 825, 19

Wood, M. L., Mann, A. W., Barber, M. G., et al. 2023, AJ, 165, 85

Wood, M. L., Mann, A. W., & Kraus, A. L. 2021, AJ, 162, 128

Wright, J. T., & Eastman, J. D. 2014, PASP, 126, 838

Wu, Y., & Lithwick, Y. 2013, ApJ, 772, 74

Zeng, L., Jacobsen, S. B., Sasselov, D. D., et al. 2019, PNAS, 116 9723

Zhou, G., Winn, J. N., Newton, E. R., et al. 2020, ApJL, 892, L21

Ziegler, C., Law, N. M., Baranec, C., et al. 2018, AJ, 156, 259